

Corrosion Study of Current Collectors for Magnesium Batteries

Laurin Rademacher,^{*[a]} Joachim Häcker,^[a] J. Alberto Blázquez,^[c] Maryam Nojabaee,^[a] and K. Andreas Friedrich^[a, b]

For rechargeable magnesium batteries, chlorine-containing electrolytes are used because chlorine species reduce the energy barrier for the intercalation process at the cathode. However, these species can cause corrosion of the cathode-side current collectors during polarization. In this study, carbon-coated aluminum and Nickel metal substrates, as well as a graphite foil, were investigated using Linear Sweep Voltammetry, Chronoamperometry, and Electrochemical Impedance Spectroscopy to evaluate their potential as current collectors in APC electrolyte. The graphite-based current collector withstood

corrosive environments at polarization potentials up to 2 V, displaying passivating behavior comparable to platinum in Chronoamperometry measurements. During Electrochemical Impedance Spectroscopy measurements, the graphite foil exhibited exceptionally high polarization resistance of at least $4.5 \text{ M}\Omega\text{cm}^2$. Combined with its low areal density of 5 mg/cm^2 , this makes it an excellent current collector material for rechargeable magnesium batteries with chlorine-containing electrolytes. In contrast, Al foil are instable towards corrosion – despite protective coatings.

Introduction

Over the last decade, the demand for energy storage systems has grown exponentially due to zero-emission electromobility, large-scale renewable energy storage, and portable consumer electronics. Lithium-ion batteries (LIBs) have emerged as a leading solution because of their high efficiency and long lifespan, but rising costs and volatility of essential minerals have presented significant challenges. Rechargeable magnesium batteries (RMB) are emerging as a promising alternative due to the high abundance and cost-effectiveness of magnesium, enhanced safety performance, and similar manufacturing processes to LIBs. This positions MIBs as direct potential competitors to LIBs in the future. Despite demonstrating feasibility at the laboratory scale, RMBs face significant challenges due to their low technology readiness level (TRL 1–3). Major issues include the lack of stable electrolyte solutions, advanced cathode materials with sufficient specific capacity, and current collectors with adequate electrochemical stability in common chloride salt-based electrolytes. Promising candidates for intercalation materials are Prussian blue analogue materials,^[1–5] V_2O_5 ^[6] which

showed a capacity of 48.3 mAh/g^{-1} ^[7] at 2.99 V (vs. Mg/Mg²⁺) or the Chevrel phase Mo_6S_8 with a theoretical capacity of 129 mAh/g^{-1} between 1 V and 1.3 V.^[8–10]

Numerous challenges of the rechargeable magnesium batteries result from the high charge density of the magnesium cations, e.g. very slow diffusion in intercalation compounds named above.^[9,11] It was demonstrated in the past that the presence of chlorine anions in the electrolyte plays a crucial role for the processes both on anode and cathode side in a magnesium battery.^[12–14] At the anode the presence of chlorine improves the electrochemical reaction kinetics and reduces the overpotentials for the deposition and dissolution of magnesium.^[15] On the cathode side, adsorbed Cl-containing complexes reduce the activation energy for the interfacial charge transfer.^[10] This allows a faster charge transfer process a the solid-solution interface.

The primary drawback of the presence of chlorine species is the increased risk of corrosion to common cell components. Muldoon et al.^[16] concluded that the corrosive nature of magnesium electrolytes is primarily due to this chlorine environment. Several studies have demonstrated severe corrosion of current collectors (CC), highlighting the need to identify suitable corrosion-resistant materials.^[1,17,18]

A very limited anodic stability of 0.7 V for aluminum, 1.0 V for stainless steel and 1.7 V for copper in tetrahydrofuran using ethylmagnesium chloride and aluminum chloride based electrolytes was reported.^[17] A stability of 2.2 V for Nickel was found by Lv et al. in magnesium organohalo-aluminate electrolyte.^[19] The carbon coating on a Nickel current collector revealed a slightly higher corrosion pit initiation potential of 2.25 V in APC electrolyte.^[20] Cheng et al.^[21] found a good stability of molybdenum (Mo) and tungsten (W) in APC electrolyte up to 2.8 V in CV measurements. However, the high densities of these elements 10.28 g cm^{-3} and 19.25 g cm^{-3} make them unsuitable for high energy density magnesium batteries. Wall et al. found a good

[a] L. Rademacher, J. Häcker, Dr. M. Nojabaee, Prof. K. A. Friedrich
German Aerospace Center (DLR),
Pfaffenwaldring 38–40, 70569, Stuttgart, Germany
E-mail: laurin.rademacher@dlr.de

[b] Prof. K. A. Friedrich
University of Stuttgart, Institute of Building Energetics, Thermal Engineering and Energy Storage (IGTE), Pfaffenwaldring 31, 70569, Stuttgart, Germany

[c] Dr. J. A. Blázquez
CIDETEC, Basque Research and Technology Alliance (BRTA), P.O. Miramon, 196, 20014 Donostia-San Sebastian, Spain

© 2024 The Authors. *Batteries & Supercaps* published by Wiley-VCH GmbH. This is an open access article under the terms of the Creative Commons Attribution Non-Commercial License, which permits use, distribution and reproduction in any medium, provided the original work is properly cited and is not used for commercial purposes.

stability of different steels and graphite based current collectors in 1 M solution of $(\text{HMDS})_2\text{Mg} - \text{AlCl}_3$.^[22] In LSV measurements they found an stability of a carbon coated aluminum current collector of 3.0 V. Inconel 625 and Hastelloy B revealed a stability of 3.3 V and 3.8 V during LSV scans and 2.5 V and 2.8 V during CA measurements for 48 h. Graphite foil disks, that were not further specified, were used as electrode protection and showed a stability of around 3.1 V during LSV scans. In a recent study^[23] Maddegalla et al. used Atomic Layer Deposition (ALD) to coat thin films of Al_2O_3 on metallic current collectors. The film was coated on a Nickel and carbon coated aluminum current collector and revealed a stability of 2.56 V and 2.8 V. A systematic overview of different corrosion studies of current collectors for magnesium batteries is summarized in the supplementary.

In this work we study the corrosion of different potential current collector foils including silver (Ag), bare aluminum (Al), Nickel (Ni), carbon coated Nickel (Ni-C), graphite (Gr) and platinum (Pt). In addition three different carbon coated aluminum foils denoted Al-GA, Al-H, and Al-HC were used, wherein Al-HC is the calendered version of Al-H. Moreover, some gold coatings on the bare aluminum foil (Al-Au) and the graphite foil (Gr-Au) were tested using a combination of electrochemical characterizations including Linear Sweep Voltammetry (LSV), Chronoamperometry (CA)^[24] and Electrochemical Impedance Spectroscopy (EIS). LSV and EIS measurements

enabled a first screening of potential options whereby the most promising candidates underwent a more thorough examination employing CA measurements. To this end, the stability over a 100 hour period at a polarization potential of 2 V is investigated. In addition, the CA measurements were coupled to EIS elucidating ongoing corrosion processes.^[25–27] From the fitted EIS spectra the polarization resistance R_p was extracted.^[27–29]

Results and Discussion

The potential substrates for use as current collectors are initially investigated by LSV measurements in APC (0.25 M $\text{AlCl}_3 + 0.5$ M Phenylmagnesium chloride (PhMgCl) in THF) electrolyte. In the frame of this work the onset potential point was defined at a current density of $10 \mu\text{A}/\text{cm}^2$. The results from the LSV scans are shown in Figures 1(a) to 1(c) for the bare metals and carbon coatings. The results for the gold coatings are depicted in Figure S1.

The Al CC exhibits the lowest onset potential of approx. 0.94 V. The gold coated aluminum foil Al-Au revealed only some slight improvement and the onset potential was increased to 1.29 V. The gold coating seems to suppress the corrosion of the Al CC up to 2.7 V to some extent. On the other hand the gold coating on the graphite CC Gr-Au reduced the stability of the graphite CC slightly from 2.92 V to 2.63 V. The

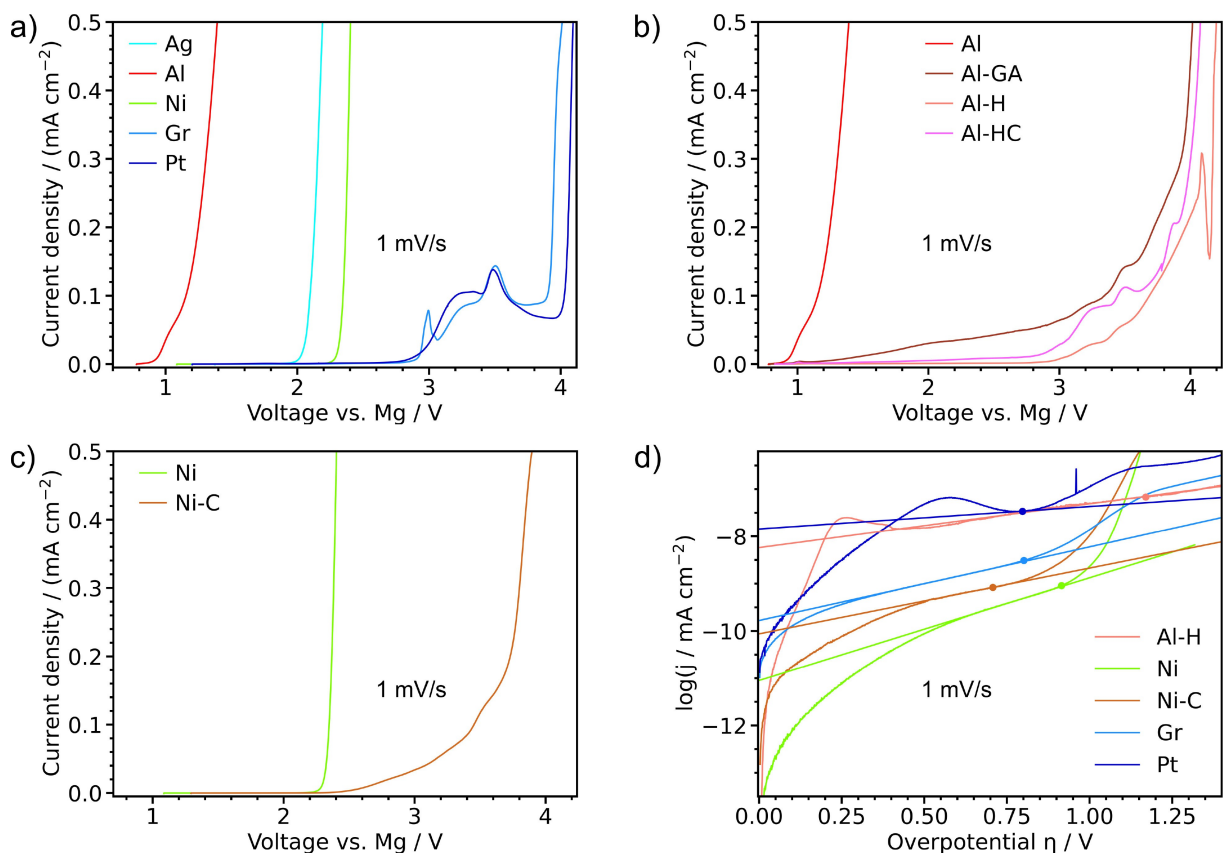


Figure 1. a) LSV screening of different CC materials; b) LSV screening of different carbon coated aluminum foils; c) LSV scan of Nickel and carbon coated Nickel CC; d) Tafel plot with fits.

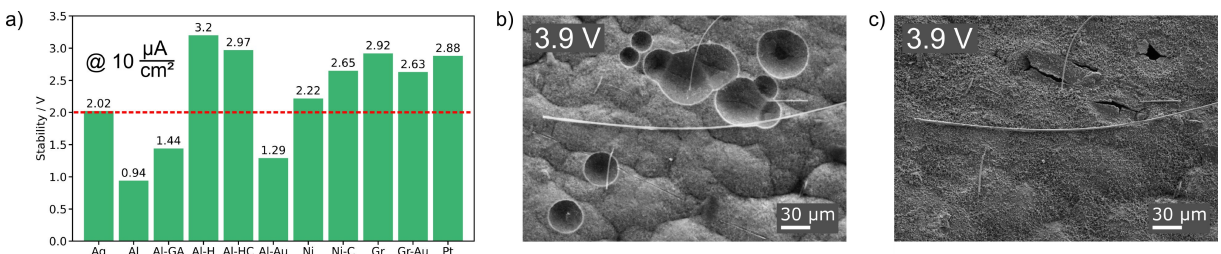


Figure 2. a) Potential onset points were obtained from the LSV curve at a current density of $10 \mu\text{A cm}^{-2}$; b) SEM of the carbon coated Nickel CC. At an acceleration voltage of 2 kV the surface of the carbon coating is visible. By increasing the voltage to 20 kV the underlaying Nickel and pitting holes can be made visible in c).

carbon coating on the Nickel Ni-C suppressed the corrosion current of the Nickel and improved the stability of the Ni CC 2.22 V to 2.65 V. Ag had a slightly lower stability than the Ni CC. The Gr revealed a similar stability like Pt which was used as a reference material. In addition the current-potential plot of the different carbon coated aluminum CC are depicted in Figure 1(b), which indicates the Al-H CC to exhibit current densities as low as the Gr CC. The calendered CC Al-HC revealed a slightly higher corrosion current during LSV experiments compared to the Al-H CC. As becomes apparent from the EDX data in supplementary S3–S5 and the cross section in S9–S11 this behavior is directly linked to the thickness of the carbon coating. Al-GA has a maximum coating thickness of 400 nm and the lowest stability of 1.44 V. Al-HC and Al-H have a coating thickness of 1.5 μm and 2.4 μm with a stability of 2.97 V and 3.2 V. This shows that a higher carbon loading results in a stronger suppression of corrosion currents. The results from the LSV scans are summarized in Figure 2(a). During this work a minimum stability of 2 V was defined which is indicated by the red dashed line. This is sufficient for most current cathode materials like the Chevrel phase Mo_6S_8 with a potential around 1.3 V.

From the logarithmic data of the LSV curve the Tafel plot in Figure 1(d) was obtained. The anodic part of the Butler-Volmer equation was fitted to the anodic Tafel region in the linear domain around 2 V vs. Mg. To obtain the equilibrium potential the cell was rest for 2 h after assembly and the open circuit potential (OCP) was recorded. The terminal potential after 2 h was used as OCP to calculate the overpotential η from the LSV electrode potential U with $\eta = U - \text{OCP}$. The dots indicate the overpotential at an electrode potential of $U=2$ V which was used for the fitting curves and CA measurements later in this study. During the fitting procedure the temperature was set to 25 °C, the results are outlined in Table 1 below. Ni-C shows a larger exchange current density compared to Ni which is caused by the increased surface area of the carbon coating. The Gr and the Ni-C CC exhibit similar exchange current densities. Among the Al based current collectors pure Al shows the largest value for j_0 due to its low corrosion resistance. For the carbon coated Al CC Al-GA shows the largest exchange current density j_0 and is well in accordance with its low LSV potential onset. Al-H exhibits the lowest exchange current density and largest LSV onset potential. Al-HC lies in between Al-GA and Al-H for both the exchange current density and the LSV potential onset. The

Table 1. Results of the anodic Butler-Volmer fit.

	$j_0/(\text{nA cm}^{-2})$	$\alpha \cdot z$	α	OCP/V
Ag	$4.1 \cdot 10^{-5}$	0.7671	0.7671	1.374
Al	6560.66	0.1866	0.0622	0.779
Al-GA	2913.36	0.0516	0.0172	0.789
Al-H	268.01	0.0237	0.0079	0.830
Al-HC	1095.15	0.0341	0.0114	0.827
Al-Au	2321.84	0.0790	0.0263	0.817
Ni	15.91	0.0558	0.0279	1.085
Ni-C	42.73	0.0357	0.0179	1.293
Gr	56.63	0.0399	–	1.199
Gr-Au	0.11	0.2483	–	1.053
Pt	391.64	0.0122	–	1.203

gold coating of Al-Au is able to reduce j_0 compared to pure Al. Pure silver is showing the lowest value of j_0 . A change of the Tafel slope can be caused by mass transport which leads to a local depletion or accumulation of reagents at the surface.^[30] Since the structure of APC is quite complex, this can result in different coverage rates of the specific species that adsorb at the surface dependent on the potential. The different species and coverage rates lead to different Tafel slopes and charge transfers processes.^[31] In case of Nickel the Cl^- species seem to accumulate at lower potentials at the surface. Hence the dissolution of Nickel is the rate determining process. When the potential is further increased, the electrolyte starts to decompose and the additional process results in a change of the Tafel slope. The organic components of the electrolyte typically show a larger stability and start to decompose at higher potentials. This can be seen by the residues on the Gr and Pt current collector in Figures S7 and S8 that experience larger potentials during the LSV measurements compared to Nickel.

During the analysis of the SEM images special attention must be given to the carbon-coated materials. As can be seen from the SEM results in Figure 2(b) and 2(c) the pitting corrosion of the Nickel was masked by the carbon coating. By increasing the beam energy from 2 keV to 20 keV it is possible to reveal the hidden pitting holes. Pitting corrosion was found on both Ni CC and the Ni-C CC as depicted in the SEM images

in Figure 3. The larger pitting holes of the carbon coated Ni CC can be explained with the larger amount of cumulated charge during the LSV scan.

The dissolution of the Nickel is the dominating corrosion process at the Nickel surface which is described by:



Due to the larger thickness of the carbon coatings on the aluminum current collectors, increasing the beam energy did not work. In their case the surface was rubbed with a piece of cotton and exfoliated with some duct tape. Despite their high onset potential of around 3 V the SEM images in Figure 4 reveal large pitting holes of up to 100 μm for Al-GA, Al-H and Al-HC CC. The dissolution reaction for the corrosion process at the aluminum surface is given by:



From the number of charges involved in the metal dissolution according to Eqs. (1) and (2) the charge transfer coefficients α were determined and are listed in Table 1. Since all values are far away from 0.5 and close to zero this indicates a highly asymmetric energy barrier with a shallow accent and very steep descent for the corrosion process.^[32] This indicates that the dissolution reaction is much more likely than the reverse reaction. Only the graphite CC withstands high corrosion rates of 500 $\mu\text{A}/\text{cm}^2$ and a potential of 4 V without

showing any signs of pitting corrosion. For this CC the dominating process was the electrolyte decomposition. As depicted in Figure 3 the decomposition occurred at points where the glass fibers of the separator got into contact with the surface of the CC. The results from the EDX measurements of the residues on Gr and Pt CC in Figures S5 and S6 are outlined in Table 2. The solid residues of the decomposed electrolyte primarily consist of magnesium, chlorine and oxygen. From the fraction of the decomposition products of chlorine:magnesium $n_{\text{Cl}}/n_{\text{Mg}}$ it becomes apparent that the main species present in solution is Mg_2Cl_3^+ which is consistent with Ref. [33]. Since THF is the only ingredient of the electrolyte which contains oxygen, the oxygen must originate from the decomposition of THF. After the cracking of the ring and removal of the oxygen the remaining carbon chain residues do not accumulate on the surface. This is confirmed by the low carbon:oxygen ratio $n_{\text{C}}/n_{\text{O}}$ between 0.32 and 0.5 found in the residues. For the full decomposition of THF into solid carbon this should be 4. From the fraction $n_{\text{O}}/n_{\text{Mg}}$ it can be seen that every Mg_2Cl_3^+ cation is coordinated by 6–10 molecules of THF. The dominant aluminum species in the APC electrolyte are PhAlCl_3^- anions.^[33] The breaking of the Al-C bond between the phenyl ring and the central aluminum ion results in the formation of benzene which was detected by Pour et al. in NMR measurements.^[33] Due to high solubility of AlCl_3 in THF almost no aluminum precipitates can be found. The different corrosion mechanisms are depicted in Figures 5(c) to 5(e).

In addition to the LSV scans EIS was used to study the corrosion behavior of the different current collector materials. The potentiostatic EIS scans were conducted prior to and after the LSV scan at an open cell voltage (OCV) before and at 2 V after the LSV scan. The results of the EIS measurements both

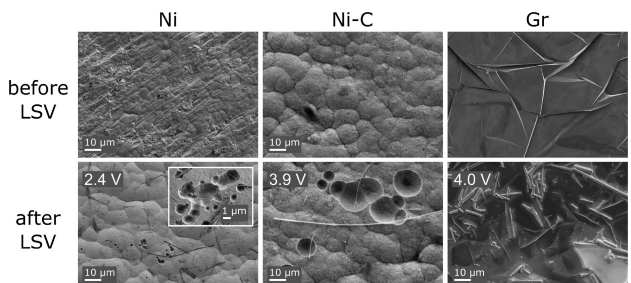


Figure 3. SEM images of Nickel (Ni), carbon coated Nickel (Ni-C) and graphite (Gr) CC in APC electrolyte after LSV experiment. The sweep was stopped at a current density of 500 $\mu\text{A}/\text{cm}^2$, the corresponding potential is shown in a image.

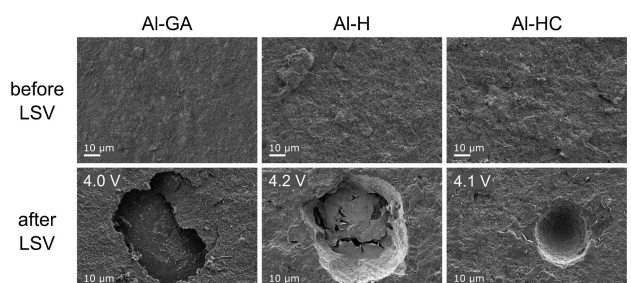


Figure 4. SEM images of different carbon coated aluminum CC in APC electrolyte; Al-H: carbon coated Al CC; Al-HC: calendered version of Al-H; The sweep was stopped at a current density of 500 $\mu\text{A}/\text{cm}^2$, the corresponding potential is shown in the image.

Table 2. Results from EDX measurements after LSV scans.

	$n_{\text{Cl}}/n_{\text{Mg}}$	$n_{\text{O}}/n_{\text{Mg}}$	$n_{\text{C}}/n_{\text{O}}$
Gr	1.65	4.73	0.50
Pt	1.49	3.12	0.32

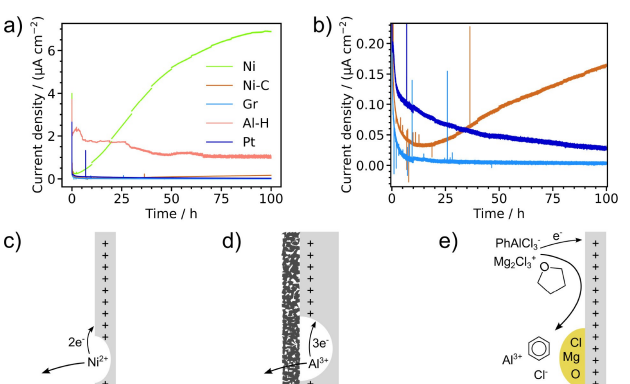


Figure 5. a) CA measurement at a polarization potential of 2 V in APC electrolyte; b) shows the zoomed data of a); c) Pitting corrosion on Nickel CC; d) Pitting corrosion under a carbon coating as observed on coated Ni and Al CC; e) Decomposition of the APC electrolyte as observed on the Gr and Pt CC.

pre and post LSV measurement are summarized in Table 3. The impedance values of the polarization resistance R_p shown here are extracted from the DC limit and show the impedance in the lower limit of the frequency.^[27,28] It becomes apparent that the most materials exhibit a considerable decline in polarization resistance. Pure aluminum shows the lowest value of polarization resistance of $2.4 \text{ k}\Omega\text{cm}^2$ at 2 V. The carbon coating of Al-GA is able to improve the polarization resistance by around one order of magnitude. Al-H has the highest value of R_p among the carbon-coated aluminum current collectors. The calendering of this CC significantly reduces the polarization resistance of Al-HC at both OCV and at 2 V which is consistent with the greater corrosion currents that were observed during LSV scans. The gold coating of the aluminum current collector Al-Au exhibits a R_p value at OCV that is similar to Al-GA. During polarization R_p drops to a value slightly larger than for pure aluminum. Remarkable is the large polarization resistance of Nickel under OCV condition which shows the largest value of all materials. Astonishing is the fact that the value is even one order of magnitude larger compared to the noble platinum. However, it experiences a dramatic drop upon polarization at 2 V. The high initial value of R_p at OCV is most likely due to some residues from the production process of the Nickel foil and uniformly covers the surface. As one can see in Figure 3 the grains on the surface of the Nickel are hidden. Upon polarization the coating

is removed and the grains become visible and the polarization resistance experiences a dramatic drop from $15951.3 \text{ k}\Omega\text{cm}^2$ to $56.1 \text{ k}\Omega\text{cm}^2$. The carbon coating on the Ni-C current collector has a lower polarization resistance at OCV than the Nickle with its residues. It has still the second highest value among all materials, especially it exceeds the value of platinum at OCV. At a potential of 2 V the polarization resistance of Ni-C drops to a value close to carbon coated aluminum Al-HC. The only two samples which show an increase of R_p during polarization are platinum and the graphitic foil. This is a hint for a good passivating behavior of those materials.

To get a better understanding of the long-term corrosion behavior Al-H, Ni, Ni-C and Gr were selected as the most promising candidates for more in depth studies due their high onset potential points, large polarization resistance and high availability. In order to investigate the long term stability of the most promising materials, CA measurements for Al-H, Ni, Ni-C, Gr and Pt CC were performed at a polarization potential of 2 V vs. Mg. In addition potentiostatic EIS spectra were recorded at 2 V every 10 h. The outcomes of the CA measurements in Figure 5 demonstrate the passivating behavior of Gr CC with the lowest corrosion current of 3 nA/cm^2 after 100 h. This behavior is comparable to that of platinum, which, however, shows a greater corrosion current over the 100 h period. The corrosion current of the Ni CC shows a passivating behavior during the first 5 h. This trend is followed by an increasing corrosion current which levels out at $6.9 \mu\text{A/cm}^2$ near the end. It shows the largest corrosion current among all materials after 100 h. The corrosion on the Nickel CC is strongly suppressed by the carbon coating of the Ni-C CC. The general trend is identical to the pure Nickel CC, however the minimum of the corrosion current is reached after 10 h. The final value of the corrosion current at the end of the CA measurement is $0.2 \mu\text{A/cm}^2$. The trend of the Al-H CC shows a slightly decreasing corrosion current and an increasing noise level. The corrosion current shows a plateau value of $1 \mu\text{A/cm}^2$.

The results from the time dependent EIS measurements are displayed in Figure 6, the spectra outlined here were fitted with the RelaxIS software. Due to the large noise level of the Al-H CC the spectra were corrected with ZHIT using the LOESS smoothing algorithm, a smoothing factor of 0.25 and the Akima spline type. The corrosion model in Figure 6(c) with two nested constant phase elements and a Warburg diffusion element was fitted to the spectra. The nested structure of two RC-elements is commonly used in literature to describe corrosion phenomena^[25,27] and was used by Zhang and Jow to describe the corrosion of an copper current collector in an lithium-ion battery.^[34] The Warburg diffusion was not visible in the spectra of Ni so the circuit element was omitted for these spectra.

The time evolution of the fitted polarization resistance R_p is shown in Figure 7(a). As depicted, the Gr CC shows the largest polarization resistance and hence corrosion resistivity. The Ni and Ni-C CC exhibit a decreasing polarization resistance, which is also indicated by a decreasing diameter of the semicircles in Figure 6. The platinum is shown for reference since it is the most noble material and has a truly passivating behavior. The uncompensated resistance R_u in Figure 7(b) describes the

Table 3. Results from LSV and EIS measurements. The EIS measurements were carried out at OCV before the LSV measurement and at 2 V after LSV.			
Material	LSV Onset/V	U_{cor}/V	$R_p/(\text{k}\Omega\text{cm}^2)$
Ag	2.02	OCV	874.3
		2	28.6
Al	0.94	OCV	131.6
		2	2.4
Al-GA	1.44	OCV	355.7
		2	37.5
Al-H	3.20	OCV	2978.7
		2	994.1
Al-HC	2.97	OCV	839.3
		2	160.9
Al-Au	1.29	OCV	473.5
		2	7.3
Nickel	2.22	OCV	15951.3
		2	56.1
Ni-C	2.65	OCV	4588.2
		2	157.4
Gr	2.92	OCV	3038.8
		2	5307.4
Gr-Au	2.63	OCV	1485.5
		2	138.5
Pt	2.98	OCV	1533.7
		2	6636.2

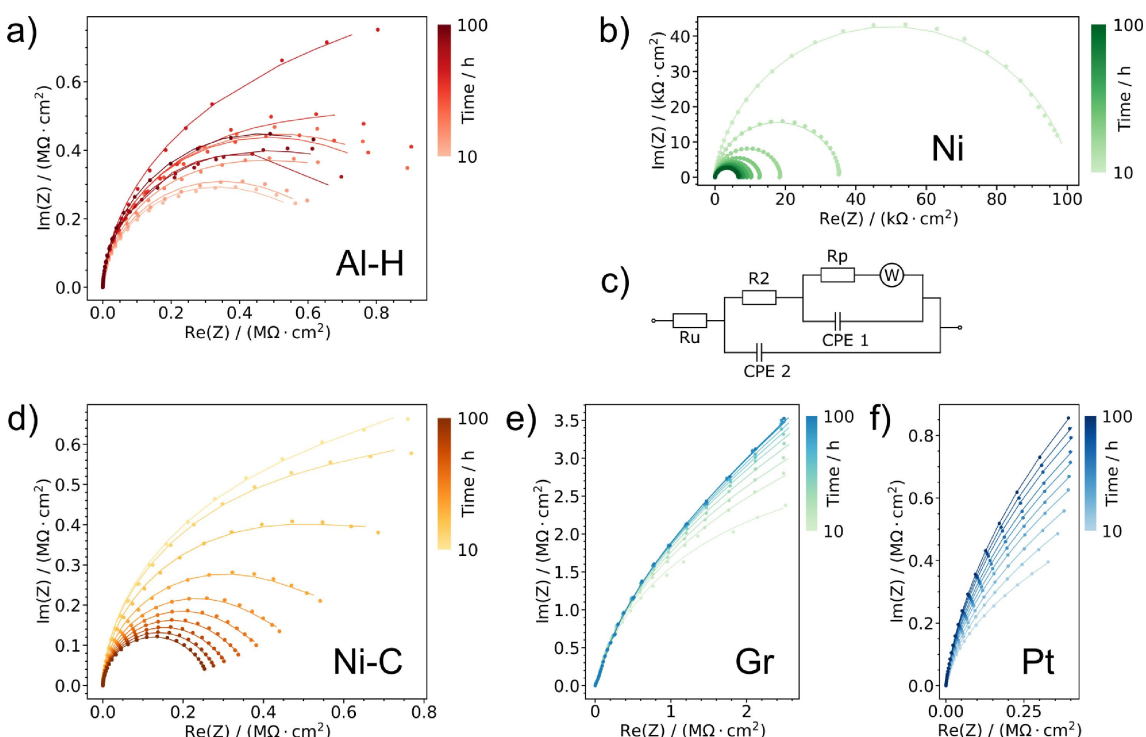


Figure 6. Nyquist diagrams of the different CC. a) Al-H shows large noise which is also reflected in CA measurements. c) Equivalent circuit which was used to model the spectra. The Warburg element was only present for Ni-C, Gr & Pt; b,d) Ni and Ni-C show decreasing diameter of the semi-circle .The diffusion contribution on the Ni-C CC is declining upon polarization. e,f) Pt and Gr show an increasing resistivity due to passivation.

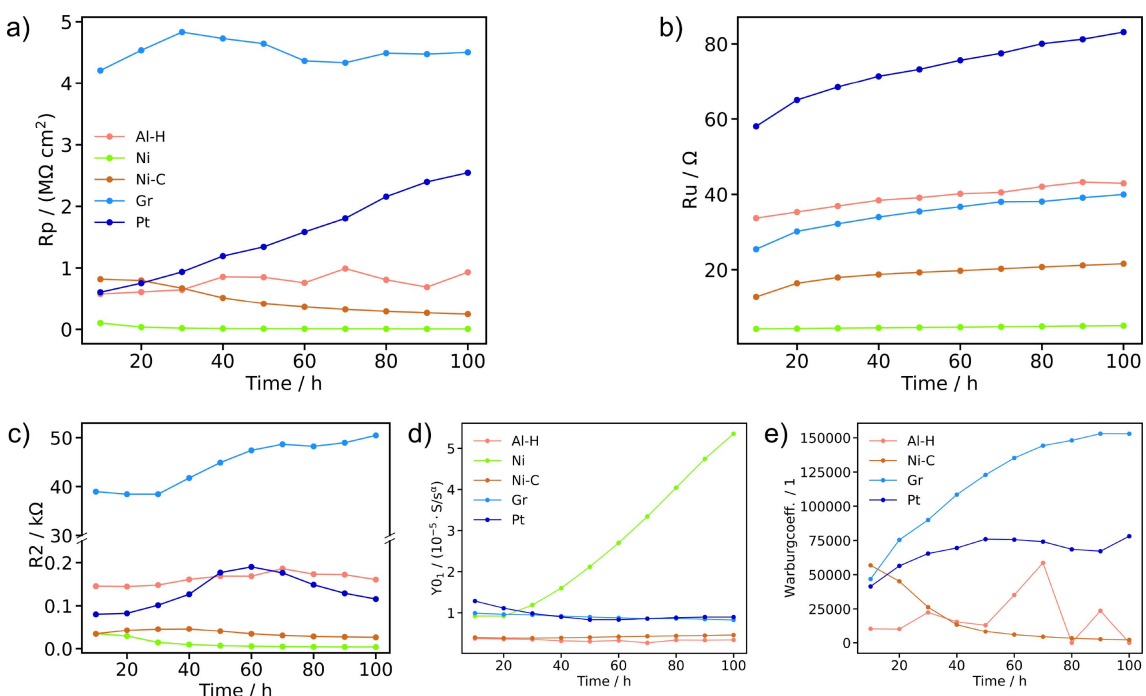


Figure 7. Results of the fitted EIS spectra. a) Polarization resistance Rp ; b) Uncompensated resistance Ru of the electrolyte; c) Dominant R_2 of the Gr CC; d) CPE 1; e) Warburg coefficient.

resistance of the electrolyte. Its increasing value is caused by a charge depletion of the electrolyte during polarization. Nickel shows the smallest electrolyte resistance. The high corrosion current of Nickel found in the CA measurements above leads to

a dissolution of Nickel according to Eq. (1). The Ni^{2+} -ions increase the conductivity which results in a low electrolyte resistance. The suppressed Ni dissolution on the Ni-C CC is reflected in a higher electrolyte resistance compared to pure Ni.

For the passivating CC no reactions at the surface take place which means that the diffusion becomes the dominant effect. This is also reflected by the increasing Warburg coefficients in Figure 7(e). For all metallic samples R2 shows a two to three orders of magnitude smaller values as the graphite CC. This element can most likely be ascribed to some solid coatings^[25,35] or adsorbed species at the surface of the current collector.^[25,28,34] Solid residues can be seen in the SEM pictures of the Al-H and Pt CC in Figure 8. The pristine Nickel CC shows some film on the surface before CA that hides the grains. After CA the film is removed from the surface of the pristine Ni CC and the grains become more pronounced. This is also reflected by the decreasing value of R2 during the first 40 h. The removal of the coating on the Ni CC was also observed after LSV experiments in Figure 3. In addition the SEM pictures reveal pitting corrosion on the Al-H and Ni CC after a polarization at 2 V for 100 h. No pitting corrosion was found for the Ni-C and Gr CC. The increasing surface roughness of the Ni CC due to pitting corrosion is also reflected by the increasing value of the capacitance Y01.^[36]

Conclusions

This study demonstrated the superior corrosion resistance of carbon-coated Nickel and graphitic current collector foils in comparison with other reported materials. Linear sweep voltammetry (LSV), electrochemical impedance spectroscopy (EIS), and chronoamperometry (CA) were used to evaluate the corrosion resistance of these materials. A polarization potential of 2 V was employed for the CA analysis, though LSV results indicate that the graphitic current collector can withstand even higher polarization potentials, allowing for the use of high-potential cathode materials like V₂O₅.^[6] The analysis of corrosion products on the current collectors provided insights into the complex structure of the Grignard-based APC electrolyte.

Corrosion-resistant current collectors enable the presence of chlorine species in rechargeable magnesium batteries, which enhances the kinetics at both the anode and cathode. The low areal density of 5 mg/cm² of the graphitic current collectors contributes to good overall performance and high energy density. While carbon coatings on aluminum current collectors reduced corrosion currents to some extent, they did not fully prevent corrosion. The excellent corrosion resistance of the studied current collectors makes them suitable for advanced electrolyte systems, paving the way for practical applications of rechargeable magnesium batteries.

Experimental

Electrolyte Synthesis

For the synthesis of the APC electrolyte 0.25 M of AlCl₃ (Aldrich, anhydrous, 99.999%) was slowly added to the rigorously stirred THF (Aldrich, 99.9%, less than 20 ppm water) solvent. Afterwards 0.5 M of a 2 M phenylmagnesiumchloride (PhMgCl) solution in THF (Aldrich) was added. Due to the exothermic nature of both reactions special care has to be taken. The solution was stirred for 16 h and showed a slightly brown color.

Electrode Preparation

Pure magnesium foil (Gelon Co.) with a thickness of 100 µm was scratched with a glass slide to remove the oxide layer. Mg counter electrode discs with a diameter of 18 mm and reference electrode rings for El-Cells were punched. The electrodes for the CC were punched out of thin metal foils with thicknesses varying between 15 and 100 µm and a diameter of 18 mm. Different CC materials were used: silver foil 100 µm (Ag, Alfa Aesar), bare aluminum foil 20 µm (Al, Hydro), Nickel 19 µm (Ni, Gelon LiB), carbon coated Nickel (Ni-C, Gelon LiB) and graphite 25 µm (Gr, Graphene Laboratories Inc.). In addition three different carbon coated aluminum foils were used: Al-GA 15 µm (Gelon LiB) which contains graphitic carbon, Al-H 35 µm (Henkel), Al-HC 27 µm (Henkel),

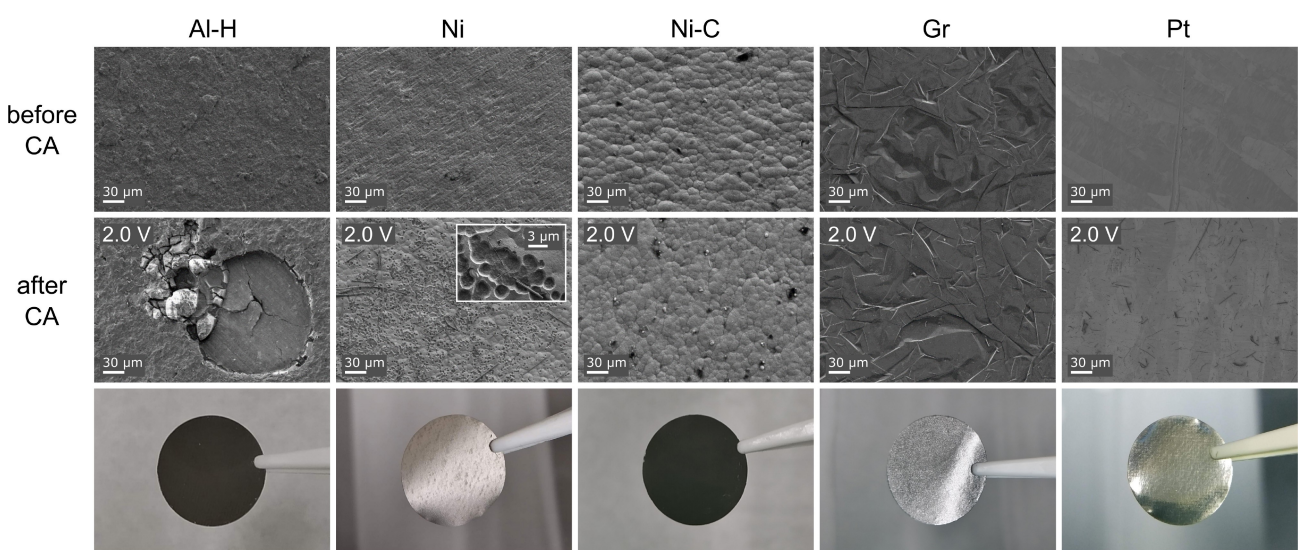


Figure 8. SEM pictures after 100 h CA measurement at a polarization potential of 2 V vs Mg. Al-H shows large holes, Ni shows small pitting holes. Ni-C, Gr and Pt remain unchanged.

wherein Al-HC is the calendered version of Al-H. The graphitic crystallites of Al-GA are embedded in a porous carbon network as can be seen in the SEM images in Figure S12. The same structural features can be observed for Al-H and Al-HC in Figure S13 and S14. Platinum foil with 100 µm (Pt) was used as a reference material due to its high corrosion stability. Moreover, some gold coatings on the bare aluminum foil (Al-Au) and the graphite foil (Gr-Au) were sputtered inhouse. The electrodes were transferred into the glovebox through a heated lock, heating was performed at 120°C overnight.

Electrochemical Characterization

For the electrochemical measurements three-electrode El-Cells were used, the cell assembly was done under argon atmosphere in a glovebox. To suppress parasitic corrosion, all steel cell parts were plated with gold galvanically or by sputtering. For the LSV measurements one layer of Whatman GF/C separator and 120 µl electrolyte was used, for the CA measurements two layers of the same separator and 200 µl electrolyte.

All electrochemical measurements were done with a Gamry Interface 1010E. The cell was located inside a Faraday cage and investigated at 25 °C. LSV scans were measured at a scan rate of 1 mV/s and started at OCV. The upper current density was limited to 500 µA/cm⁻² and the LSV scan was terminated upon reaching this value. The current limit protects the other cell parts from corrosion which might result in a misleading interpretation of the measurements. For the EIS analysis a frequency range of 20 mHz–500 kHz was used and an AC amplitude of 5 mV was employed. In addition, the EIS measurements were combined with the LSV and the CA measurement. Both the LSV and CA measurements were carried out in separate cells. To equilibrate the cells after assembly they were rest for two hours. Afterwards a potentiostatic EIS measurement was carried out at OCV followed by the LSV scan. Subsequently, an additional potentiostatic EIS measurement was carried out at a polarization potential of 2 V. For the CA measurements the cells were polarized at 2 V and potentiostatic EIS measurements were taken every 10 h at 2 V for in total 100 h.

Post Mortem Analysis

For the post mortem analysis, a Zeiss Ultra Plus SEM and Zeiss Gemini 350 were used. For the thin carbon coatings it was sufficient to increase the beam energy from 2 kV to 20 kV to penetrate through the carbon coating. For thicker coatings the carbon layer was removed mechanically by rubbing with cotton followed by exfoliation with a piece of duct tape. For the cleaning of the electrodes all samples were immersed in pure THF solvent for 30 min.

Author Contributions

Laurin Rademacher: Conceptualization, Methodology, Investigation, Formal analysis, Visualization, Writing – original draft. Joachim Häcker: Writing – review & editing. Maryam Nojabaei: Writing – review & editing, Project administration. Alberto Blázquez: Samples & review. K. Andreas Friedrich: Supervision, Validation.

Acknowledgements

This project has received funding from the European Union's Horizon 2020 research and innovation program under grant agreement No. 824066. Especially I want to thank Norbert Wagner for the fruitful discussions and methodological contributions to this work. Open Access funding enabled and organized by Projekt DEAL.

Conflict of Interests

The authors declare no conflict to finterest.

Data Availability Statement

The data that support the findings of this study are available from the corresponding author upon reasonable request.

Keywords: Current Collector • Magnesium Batteries • Corrosion • Linear Sweep Voltammetry • Chronoamperometry • Electrochemical Impedance Spectroscopy • Graphite Foil • Carbon Coating • Nickel Foil • Aluminum Foil

- [1] A. L. Lipson, S.-D. Han, B. Pan, K. A. See, A. A. Gewirth, C. Liao, J. T. Vaughan, B. J. Ingram, *J. Electrochim. Soc.* **2016**, *163*, A2253.
- [2] Y. Yang, J. Zhou, L. Wang, Z. Jiao, M. Xiao, Q. an Huang, M. Liu, Q. Shao, X. Sun, J. Zhang, Prussian blue and its analogues as cathode materials for Na-, K-, Mg-, Ca-, Zn- and Al-ion batteries **2022**, *99*, 107424.
- [3] R. Trocoli, R. Houdeville, C. Frontera, S. Vincent, J. M. Garcia Lastra, R. Palacin, *ChemSusChem* **2023**, *17*, e202301224.
- [4] L. Chen, J. L. Bao, X. Dong, D. G. Truhlar, Y. Wang, C. Wang, Y. Xia, *ACS Energy Lett.* **2017**, *2*, 1115.
- [5] D. M. Kim, Y. Kim, D. Arumugam, S. W. Woo, Y. N. Jo, M. S. Park, Y. J. Kim, N. S. Choi, K. T. Lee, *ACS Appl. Mater. Interfaces* **2016**, *8*, 8554.
- [6] W. hai Yu, D. zhi Wang, B. Zhu, G. en Zhou, *Solid State Commun.* **1987**, *63*, 1043.
- [7] M. S. Chae, J. Hyoung, M. Jang, H. Lee, S. T. Hong, *J. Power Sources* **2017**, *363*, 269.
- [8] D. Aurbach, Z. Lu, A. Schechter, Y. Gofer, H. Gizbar, R. Turgeman, Y. Cohen, M. Moshkovich, E. Levi, *Nature* **2000**, *407*, 724.
- [9] E. Levi, Y. Gofer, D. Aurbach, *Chem. Mater.* **2010**, *22*, 860.
- [10] R. Attias, M. S. Chae, B. Dlugatch, M. Oliel, Y. Goffer, D. Aurbach, *ACS Catal.* **2020**, *10*, 7773.
- [11] E. Levi, M. D. Levi, O. Chasid, D. Aurbach, *J. Electroceram.* **2009**, *22*, 13.
- [12] D. Aurbach, G. S. Suresh, E. Levi, A. Mitelman, O. Mizrahi, O. Chusid, M. Brunelli, *Adv. Mater.* **2007**, *19*, 4260.
- [13] O. Mizrahi, N. Amir, E. Pollak, O. Chusid, V. Marks, H. Gottlieb, L. Larush, E. Zinigrad, D. Aurbach, *J. Electrochim. Soc.* **2008**, *155*.
- [14] Y. S. Guo, F. Zhang, J. Yang, F. F. Wang, Y. Nuli, S. I. Hirano, *Energy Environ. Sci.* **2012**, *5*, 9100.
- [15] R. Attias, M. Salama, B. Hirsch, Y. Goffer, D. Aurbach, Anode-Electrolyte Interfaces in Secondary Magnesium Batteries, *Joule* **2019**, *3*, 27.
- [16] J. Muldoon, C. B. Bucur, A. G. Oliver, J. Zajicek, G. D. Allred, W. C. Bogess, *Energy Environ. Sci.* **2013**, *6*, 482.
- [17] S. Yagi, A. Tanaka, T. Ichitsubo, E. Matsubara, *ECS Electrochim. Lett.* **2012**, *1*, 1.
- [18] Z. Feng, Y. NuLi, J. Wang, J. Yang, *J. Electrochim. Soc.* **2006**, *153*, C689.
- [19] D. Lv, T. Xu, P. Saha, M. K. Datta, M. L. Gordin, A. Manivannan, P. N. Kumta, D. Wang, *J. Electrochim. Soc.* **2013**, *160*, A351.
- [20] S. Chakrabarty, J. A. Blázquez, T. Sharabani, A. Maddegalla, O. Leonet, I. Urdampilleta, D. Sharon, M. Noked, A. Mukherjee, *J. Electrochim. Soc.* **2021**, *168*, 080526.
- [21] Y. Cheng, T. Liu, Y. Shao, M. H. Engelhard, J. Liu, G. Li, *J. Mater. Chem. A* **2014**, *2*, 2473.

- [22] C. Wall, Z. Zhao-Karger, M. Fichtner, *ECS Electrochem. Lett.* **2015**, *4*, C8.
- [23] A. Maddegalla, Y. Kumar, S. H. Akella, S. Taragin, D. Bravo-Zhivotovskii, H. K. Sadhanala, D. Aurbach, M. Noked, *J. Electrochem. Soc.* **2024**, *171*, 020540.
- [24] S. S. Abdel Rehim, H. H. Hassan, M. A. Amin, *Corros. Sci.* **2004**, *46*, 1921.
- [25] J. M. H. Héctor Herrera Hernández, Adriana M. Ruiz Reynoso, Juan C. Trinidad González, C. O. González Morán, José G. Miranda Hernández, Araceli Mandujano Ruiz, R. O. Cruz, *Electrochemical Impedance Spectroscopy (EIS): A Review Study of Basic Aspects of the Corrosion Mechanism Applied to Steels* **2020**.
- [26] A. C. Lazanas, M. I. Prodromidis, *ACS Measurement Sci. Au* **2023**, *3*, 162.
- [27] F. Mansfeld, S. L. Jeanjaquet, M. W. Kendig, *Proc. Electrochem. Soc.* **1987**, *87-2*, 217.
- [28] J. R. Scully, The polarization resistance method for determination of instantaneous corrosion rates: A review *Corrosion* **2000**, *56*, 199.
- [29] V. Vivier, M. E. Orazem, *Chemical Reviews* **2022**, *122*, 11131.
- [30] D. Li, C. Lin, C. Batchelor-McAuley, L. Chen, R. G. Compton, *J. Electroanal. Chem.* **2018**, *826*, 117.
- [31] T. Shinagawa, A. T. Garcia-Esparza, K. Takanabe, *Sci. Rep.* **2015**, *5*, 1.
- [32] T. Sakata, H. Nakamura, *Bull. Chem. Soc. Jpn.* **2001**, *74*, 2285.
- [33] N. Pour, Y. Gofer, D. T. Major, D. Aurbach, *J. Am. Chem. Soc.* **2011**, *133*, 6270.
- [34] S. S. Zhang, T. R. Jow, *J. Power Sources* **2002**, *109*, 458.
- [35] S. Dai, J. Chen, Y. Ren, Z. Liu, J. Chen, C. Li, X. Zhang, X. Zhang, T. Zeng, *Int. J. Electrochem. Sci.* **2017**, *12*, 10589.
- [36] M. E. Orazem, I. Frateur, B. Tribollet, V. Vivier, S. Marcellin, N. Pébère, A. L. Bunge, E. A. White, D. P. Riemer, M. Musiani, *J. Electrochem. Soc.* **2013**, *160*, C215.

Manuscript received: June 17, 2024

Revised manuscript received: August 18, 2024

Accepted manuscript online: September 4, 2024

Version of record online: October 31, 2024